PHOTOLUMINESCENCE CHARACTERIZATION OF PATTERNED QUANTUM DOTS AND INVERSE QUANTUM DOTS

BY

AKASH GARG

THESIS

Submitted in partial fulfillment of the requirements
for the degree of Master of Science in Electrical and Computer Engineering
in the Graduate College of the
University of Illinois at Urbana-Champaign, 2010

Urbana, Illinois

Adviser:

Professor James J. Coleman

ABSTRACT

The ever increasing demand for oil and its limited supply have forced us to look for alternate sources of energy. Solar energy offers a cheap, alternate form of energy. The efficiency of a solar cell is set by the Shockley-Queisser limit and is currently very low. New techniques to increase the efficiency of solar cells are being explored. Quantum dots and inverse quantum dots are promising future ways to increase the efficiency of solar cells through multiple exciton generation. In this thesis, the fabrication and characterization of defect-free quantum dots and anti-dots are discussed.

ACKNOWLEDGMENTS

I first thank my adviser, Professor Jim Coleman for giving me the opportunity to join his research group. His scientific expertise and guidance made this work possible. I thank him for believing in me and my crazy ideas, whatever they were. I would like to thank my lab mates Neville Dias, Uttam Reddy, and Jonathan Young for making work a fun place. I specially thank Neville Dias and Uttam Reddy for their gracious assistance and teaching me the fundamentals of laser processing, MOCVD growth, and e-beam lithography. I thank Tonia Siuts for being very patient with the never-ending list of chemicals, wafers, etc., that needed to be ordered on a daily basis. I would also like to thank my friends Prateek, Frank, Ray, David, and Antonio for all the good times. Lastly, I would like to thank to my parents for their loving support and encouragement.

TABLE OF CONTENTS

CHAPTER 1: INTRODUCTION

The use of quantum dots in the photonic devices has revolutionized the field of semiconductor research. Quantum dots are a topic of wide research because of the superior properties they offer compared to quantum wells when employed as an active material in semiconductor lasers [1-7]. These superior properties are a result of the 3-D confinement of the electrons. 3-D confinement of the electrons leads to a delta function density of states, which results in low threshold current densities in semiconductor lasers. Lasers employing InGaAs quantum dots as active material grown on GaAs substrates have already been demonstrated to have better beam quality [8], reduced threshold, extended range of emission wavelengths [8] and operating temperature insensitivities [9]. Quantum dots are also finding their applications in single photon devices which can eventually lead to the quantum communication [10]. More recently quantum dots have been explored as an active material for solar cells with the promise of multiple exciton generation possibility [11]. In this chapter, we will give a brief introduction to solar cells and quantum dots and will discuss how the use of quantum dots can lead to the high efficiency solar cells which can break the Queisser-Shockley limit which is the maximum theoretical efficiency of a solar cell [12].

1.1 Solar Cells

A solar cell is a device that converts light energy into electrical energy. When light is absorbed by a material, photons give up their energy to excite the electrons to a high energy level. The excited electrons decay back to their ground state levels within a few picoseconds. In a solar cell, these excited electrons are extracted and fed to an external circuit before they can relax to the ground levels. The effectiveness of a solar cell depends upon how well the carriers are absorbed

and extracted. The following section will describe the brief history and underlying physics of solar cells.

1.2 History of Solar Cells

The photovoltaic effect was first demonstrated by Edmund Bequerel in 1839 when he observed the generation of electric current from a silver coated platinum electrode immersed in electrolyte on exposure to sunlight. The first working solar cell was developed by Charles Fritts in 1894 by melting a thin film of selenium between gold and another metal. In the next couple of years, the photovoltaic effect was observed in copper-copper oxide thin films, in lead sulphide films and later in thallium sulphide [13]. The most fascinating thing about the solar cell was that the total current produced was proportional to the intensity of the incident light. Also the current generated was dependent on the wavelength of the incident light, making the cells ideal for photographic light materials [13]. Modern research on solar cells began in 1939 when Russell Ohl made the first junction solar cell while investigating the use of silicon for point contact rectifiers. Solar cells saw their first application when they were used in Sputnik, the first satellite, which was fully powered by solar cells [14]. Solar cells were not seriously considered for power generation for several decades due to the high production cost of $200/W. However, the oil crisis of 1973 experienced by the western world caused a sudden growth of interest in alternative energy sources [13]. Photovoltaics became a topic of intense research and a lot of time and money were invested to find alternate materials and designs to improve the device efficiency of solar cells. Thus the modern era of solar cells started with the motivation to find cheap alternative (renewable) energy sources.

1.3 Characteristics of Solar Cells

Some of the important characteristics of a solar cell are listed below.

Photocurrent

The quantum efficiency of a solar cell is defined as the probability that a photon incident on the cell will generate an electron-hole pair that can be delivered to the external circuit. The quantum efficiency of a cell depends on the absorption coefficient of the material, the efficiency of charge separation and the efficiency of charge collection. Thus the total photocurrent density of a solar cell J_{sc} is related to quantum efficiency *QE (E)* as

$$J_{sc} = q\int b_s(E)QE(E)dE$$

where $b_s(E)$ is the photon flux density, i.e., the number of photons with energy in the range of E and $E+dE$ incident on a unit area per unit time.

Dark Current and Open Circuit Voltage

The reverse current generated in the solar cell, which reduces the photocurrent from its short circuit value whenever a load is present, is known as dark current. For an ideal diode the dark current density is given by

$$J_{dark}(V) = J_0(e^{\frac{qV}{k_BT}} - 1)$$

where J_0 is a constant, k_B is Boltzmann's constant and T is temperature in kelvins.

The net current density will be reduced from its ideal value, i.e., from the short circuit current density. Therefore, the net current density of a solar cell considering the dark current is given by

$$J = J_{sc} - J_0(e^{\frac{qV}{k_BT}} - 1)$$

The maximum potential difference across the solar cell when the contacts are open is known as the open circuit voltage. The open circuit voltage for an ideal diode is given as

$$V_{oc} = \frac{kT}{q} \ln(\frac{J_{sc}}{J_0} + 1)$$

The cell generates power when the voltage is between *0* and V_{oc} and acts as a photodetector for V<0.

Efficiency

Fill factor is defined as the output power available at the maximum operation point divided by the product of open circuit voltage and short circuit current. Fill factor is one of the important parameters in defining the overall behavior of the solar cell. The voltage at the maximum operating point is defined as V_m with corresponding current density J_m. Fill factor defines the squareness of the J-V curve and is given as

$$FF = \frac{J_m V_m}{J_{sc} V_{oc}}$$

where J_{sc} is the short circuit current and V_{oc} is the open circuit voltage. Typically the materials with high short circuit current have low open circuit voltage [12]. The efficiency of a solar cell is defined as the amount of power density delivered as a fraction of incident light power density.

$$\eta = \frac{J_m V_m}{P_s}$$

where V_m is the operating voltage at which the power obtained from the cell reaches the maximum value, J_m is the current density corresponding to the maximum power density and P_s is the power density of the incident light.

1.4 Classification of Solar Cells

Solar cells today are classified as either first, second or third generation. First generation solar cells were made from single crystal silicon or poly-grain silicon and have efficiencies up to 26% [15]. Since first generation solar cells are made from single crystal silicon, they tend to be very expensive for widespread use. To overcome the cost issues related to the first generation photovoltaics, different alternatives were explored, leading the transition to thin film solar cells, also known as second generation photovoltaics. Second generation photovoltaics consist of solar cells made from amorphous silicon, thin film silicon, $CuInSe_2$, CdTe and dye synthesized solar cells.

Second generation photovoltaics reduced the overall cost of the solar cells but at the expense of reduced efficiencies. Efficiency is mainly limited due to the poor film quality, and because very little material is used the cost of the second generation photovoltaics is much less than the first generation. The main limiting factor in the high conversion efficiency of solar cell is the loss of excess kinetic energy by phonon emission; i.e., electrons and holes lose their excessive kinetic energy in the form of heat to the lattice by phonon emission. The electrons and holes then cool down to the band edges from where they are extracted and feed to the external circuit. Figure 1 shows the relaxation of a hot electron. The motivation for third generation solar cells is to achieve efficiency > 32% (Queisser-Shockley limit) while keeping the cost very low. Different techniques are used to increase the efficiency in third generation photovoltaics, including multiple gap tandem cells, intermediate band solar cells, hot carrier solar cells and spectrum conversion solar cells. Some of the technologies are already on the market while others are still undergoing extensive research. The price of third generation photovoltaics is still very

high. The following section briefly illustrates the various third generation solar cells with some of their advantages and disadvantages.

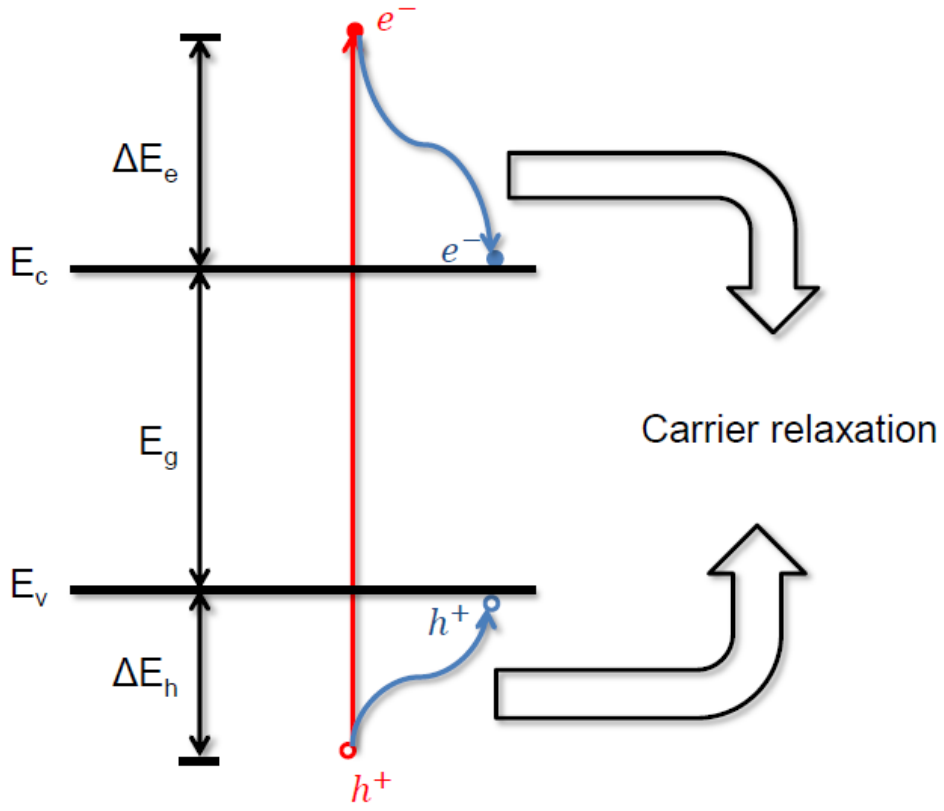

Fig. 1. Relaxation of hot carriers by phonon emission. The excess energy of the carriers is given as heat to the lattice.

Multi-Junction Solar Cells

Multi-junction solar cells at present can exceed the Queisser-Shockley limit, but they are still not very cost effective [16]. Multi-junction solar cells use different bandgap materials stacked on each other to separate the solar spectrum. The high energy photons are then absorbed by high bandgap material, and low energy photons are absorbed by low bandgap material. By stacking an infinite number of junctions, theoretically we can get efficiency of 86% under maximum solar irradiance [17]. There are two configurations in which solar cells can be stacked. In the first configuration, multiple stacks are grown on a single substrate with each p-n junction separated

from the other by a very thin tunnel injection junction. Since there are only two contacts in this structure the total current output is limited by the lowest current producing junction [18]. The excess current generated is wasted in this configuration. In the other configuration, different p-n junctions are grown on individual substrates. Contacts are formed at each junction and later the different junctions are separated from the substrate and are stacked. Since different contacts are used for each p-n junction there is no limitation on the maximum current generated by the solar cell. However, the use of different substrates increases the overall cost of the solar cell. Currently, triple junction solar cells are used to achieve efficiencies of up to 41%. InGaP/GaAs/Ge is a very common triple junction solar cell with maximum efficiency of 40.7% [19]. Also, while using a single substrate, lattice mismatch between different junctions should be kept in mind so as not to induce dislocation misfits that can greatly reduce the efficiency of solar cells.

Intermediate Band Solar Cells

Intermediate band solar cells use a single junction with narrow density of states within the bandgap to increase the overall efficiency of the solar cells. The narrow density of states within the bandgap allows sub-bandgap absorption. Figure 2 shows the band diagram of the intermediate band solar cells. The absorption can take place between the valence band and conduction band, valence band and intermediate band, and intermediate band and conduction band. Since sub-bandgap absorptions are allowed, the overall number of carriers that can be extracted from the single junction is increased. At first the intermediate band was introduced in silicon by intentionally doping it with impurities. This structure did not give any significant increase in efficiency, and so soon interest shifted towards the use of quantum dots and quantum wells as intermediate band materials. Quantum wells of lower bandgap were employed in solar

junctions to improve the efficiency through sub-bandgap absorption leading to additional electron-hole pairs, which can lead to additional photocurrent. However, a thermodynamic treatment by Marti, Laque and Cuadra has shown that the quantum wells cannot improve the efficiency of the solar cells unless photons with energy less than bandgap are absorbed in the quantum well [20]. Due to the limitations of the quantum wells, interest has shifted towards the use of quantum dots. Quantum dots have a lower bandgap than the barrier material and the energy levels for dots are discrete. If quantum dots are arranged periodically, the overlap between the discrete energy levels can lead to the formation of sub-bands [20]. There are two main requirements for the operation of IB solar cells. First, the Fermi level of the IB should lie in between the CB and VB Fermi levels so that enough transitions can be made from IB to the conduction band. Second, the absorption coefficients between the three transitions should not overlap; their overlap can reduce the electron population in the conduction band.

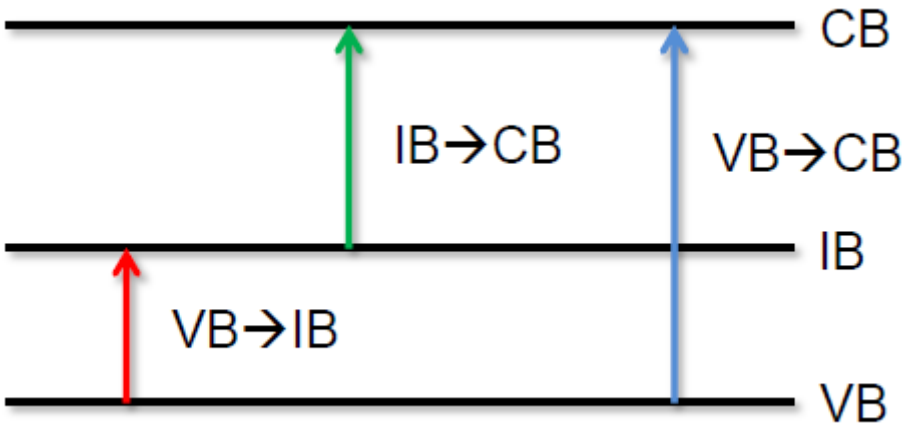

Fig. 2. Schematic of intermediate band solar cell. This configuration has available transitions from CB to VB, from VB to IB, and from IB to CB, which allows the absorption of sub-bandgap photons.

Hot Electron Solar Cells

A photon incident on a semiconductor having energy greater than the bandgap of the material will create an electron-hole pair. The excess energy of the electron is released to the lattice as heat through the optical phonon emission without serving any useful purpose. One way to utilize this excess energy is if we can extract the hot carriers before they thermalize. This is done using energy selective contacts which allow the carriers in a small energy window to leave through the metal contacts. Silicon quantum dots embedded in a SiO_2 matrix have been explored as energy selective contacts. The I-V curve of the device shows negative differential resistance at room temperature, indicating their stability for this purpose [21]. Theoretical calculations of hot carrier extraction have shown efficiency greater than 80 % is possible [22] under full solar irradiance.

Another possibility for increasing the efficiency is through multiple exciton generation. In multiple exciton generation, also known as carrier multiplication, the excess energy of hot electrons is used to create additional electron-hole pairs. The energy of the incoming photon should be at least twice the bandgap energy, and the energy separation between the conduction band subbands should be of the order of the bandgap in order to create additional electron-hole pairs. The lifetime of carriers in bulk semiconductor is of the order of few picoseconds; therefore, it is not possible to observe the carrier multiplication in bulk semiconductors. Initially quantum wells were explored as candidates for carrier multiplication. The quantum well showed an increase in carrier relaxation rate from a few picoseconds to hundreds of picosecond because of 1-D quantization [23]. However this effect is only possible under large carrier densities which are difficult to achieve under normal solar irradiance. Therefore quantum dots are suitable candidates for carrier multiplication, because 3-D quantization of electrons can decrease the carrier relaxation rate significantly. In a quantum dot the energy levels are completely discrete

and localized; if the energy between the subbands is greater than the optical phonon energy, electrons cannot relax through single phonon emission. They can relax through multiple phonon emission, but the probability of multiple phonon emission is far less than single phonon emission. This can increase the carrier relaxation rate to an order of a few nanoseconds and the process of multiple exciton generation can become much more efficient. Experiments have revealed quantum yields of 300% and 700% in PbSe and PbS quantum dots respectively [24, 25]. Electrical bias is used to extract the carriers from the quantum dots. Although experiments have demonstrated an increase is quantum yield, no working device has yet been made demonstrating multiple electron generation in solar cells.

Spectrum Conversion Solar Cells

Until now all the techniques we have discussed are focused on adjusting the bandgap of the solar material to match the spectrum of the sun. Recently, research has been done to convert the spectrum from that of the sun to one more suitable for the solar cell. In this technique, the low bandgap photons are unconverted into high energy photons and high bandgap photons are downconverted into multiple low energy photons. This process is relatively easy as it is consistent with all the existing technologies and the only changes are made to the spectrum. However, adding additional layers of up-converters or down-converters in front of a solar cell can increase the amount of light reflecting back from the solar cell, increasing the loss. Much research needs to be done in order to improve the efficiency of solar cells using spectrum conversion techniques.

From the above discussion of solar cells, it is clear that defect-free quantum dots are a key element in increasing the efficiency of solar cells. In this thesis, we will discuss some the fabrication techniques that can be used to fabricate defect-free quantum dots very reliably. Then

we will introduce a novel structure called the *inverse quantum dot* or *nanopore* that has some advantages over conventional quantum dots. Finally, in the last chapter we will discuss the experimental setup that is used to measure the emission spectrum from the patterned quantum dots and nanopore structures.

1.5 Physics of Quantum Dots

Recent advances in microfabrication technology have allowed researchers to create new quantum confinement structures which have opened the doors to a completely new physical realm. When the motion of an electron in a solid is limited to the de Broglie wavelength, quantum effects can be seen. The properties of quantum dots arise because of this size quantization. Since a quantum dot is quantized in all three dimensions, its physical properties are very similar to those of an individual atom. In a bulk material the electrons are free to move in all three dimensions with effective mass m^*. The energy of the corresponding electron is given as

$$E = \frac{\hbar^2}{2m^*}(k_x{}^2 + k_y{}^2 + k_z{}^2)$$

where k_x, k_y, and k_z are the wave vectors of electrons in the x, y and z directions respectively. Density of states is defined as the number of available states in which the carriers can exist and is proportional to the square root of energy of the electron. Since the energy spectrum of an electron in a bulk semiconductor is continuous, the density of states is also a continuous function. In a quantum well the motion of the electron is only confined in one direction, but it is still free to move in other directions. The energy of the electron in a quantum well is given as

$$E = \frac{\hbar^2}{2m^*}(k_x{}^2 + k_y{}^2) + \frac{l^2\Pi^2\hbar^2}{2m^* L_z{}^2}$$

The density of states is greatly modified from bulk to 1-D confinement as it behaves like a step function near the quantization energies. Confinement of electrons in the case of a nanowire, i.e. 2-D confinement, allows electrons to move freely only in one direction with energy

$$E = \frac{\hbar^2}{2m^*} k_x^{\,2} + \frac{m^2\Pi^2\hbar^2}{2m^* L_y^{\,2}} + \frac{l^2\Pi^2\hbar^2}{2m^* L_z^{\,2}}$$

In this case the density of states is highly peaked at the quantized energy levels, and at all other energies it is different. And when the motion of the electron is completely confined in all three dimensions, as in quantum dots, the energy spectrum becomes completely discrete as given by

$$E = \frac{n^2\Pi^2\hbar^2}{2m^* L_x^{\,2}} + \frac{m^2\Pi^2\hbar^2}{2m^* L_y^{\,2}} + \frac{l^2\Pi^2\hbar^2}{2m^* L_z^{\,2}}$$

The density of states of a quantum dot becomes a delta function with some finite broadening. Figure 3 shows the evolution of density of states from a bulk semiconductor to a quantum dot. Since in a quantum dot the densities of states are discrete delta functions, those states can be populated easily with little applied current.

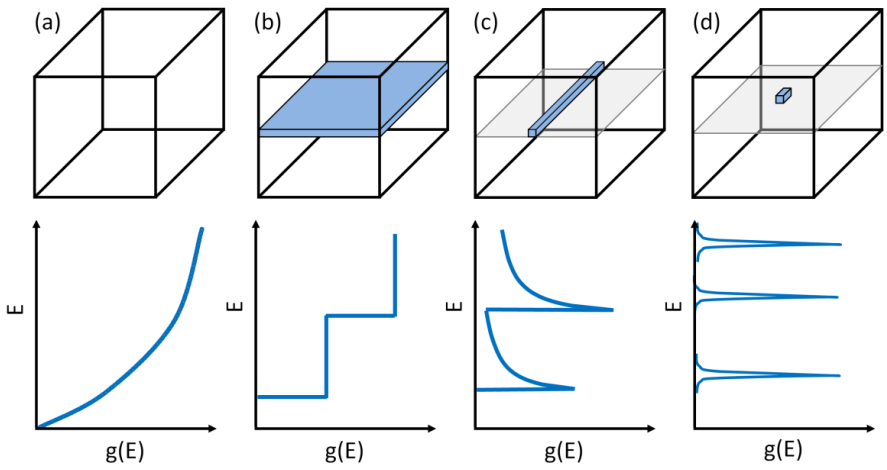

Fig. 3. Evolution of density of states from bulk semiconductor to 3-D confined quantum dots.

This property becomes very important for quantum dot lasers which have low threshold current densities compared to quantum well lasers. Also, because of the discrete energy states, the carrier

relaxation rate in quantum dots is much lower than in the bulk, 1-D and 2-D confined structures. This effect can eventually lead to multiple exciton generation, better known as carrier multiplication.

Additional degrees of quantization have proven harder to obtain. The quantum well was made possible because epitaxy allowed control at an atomic scale. The additional two dimensions, however, are not necessarily related to growth but often rather to processing in the plane of a structure. In this thesis we will discuss some of the fabrication techniques that can be used to achieve the additional degrees of quantization with great reliability.

CHAPTER 2: FABRICATION

Quantum dots offer a variety of applications in photonic and photovoltaic devices as discussed in the previous chapter. However, in order to fully utilize the properties of quantum dots, precise control over their size and composition is needed. The simplest and easiest way to grow a quantum dot is by self-assembled growth, but this method offers neither composition control nor control over the position of dots. In this chapter, a technique known as selective area epitaxy will be discussed which offers a precise control over the positioning of the dots. In addition, the technique offers composition and growth enhancement as reported by others [26]. Thus a wet etch technique using titanium as etch mask will be discussed, which removes the growth and composition enhancement. Later a new wet etch technique will be discussed that offers improved uniformity in dot size over a large area compared to wet etch dots fabricated using titanium as etch mask. At the end the chapter, fabrication techniques for the new nanostructure, the inverse quantum dot or nanopore, will be discussed.

2.1 Self-Assembled Growth

In the growth of epitaxial heterostructures, depending on the lattice mismatch and surface energy, three different growth modes can occur: Frank van der Merwe, Volmer-Weber and Stranski-Krastanow. Each mode growth depends on the lattice mismatch and surface energy. Frank van der Merwe, or layer-by-layer, growth mode will result if the sum of epilayer surface energy and surface energy is less than substrate surface energy. Volmer-Weber, or island, growth mode occurs if there is any change in the surface energy. Stranski-Krastanow growth mode occurs for a lattice mismatched strained system. Depending upon the material system, for Stranski- Krastanow growth mode there is a critical thickness up to which the normal layer-by-layer growth occurs, but beyond which the additional strain of the system is released by

formation of islands called quantum dots. The size and positioning of dots in this mode is largely random. The first studies of self-assembled quantum dots were done using molecular beam epitaxy [27], but later, formation was also shown with metal-organic chemical vapor deposition (MOCVD) [28]. Present day technologies show the growth of defect-free self-assembled dots with densities of 10^{10}-10^{11} cm^{-2} [29]. Linewidths as small as 20 meV have been demonstrated from the self-assembled dots [30]. Figure 4 shows the scanning electron microscopic image of the self-assembled dots.

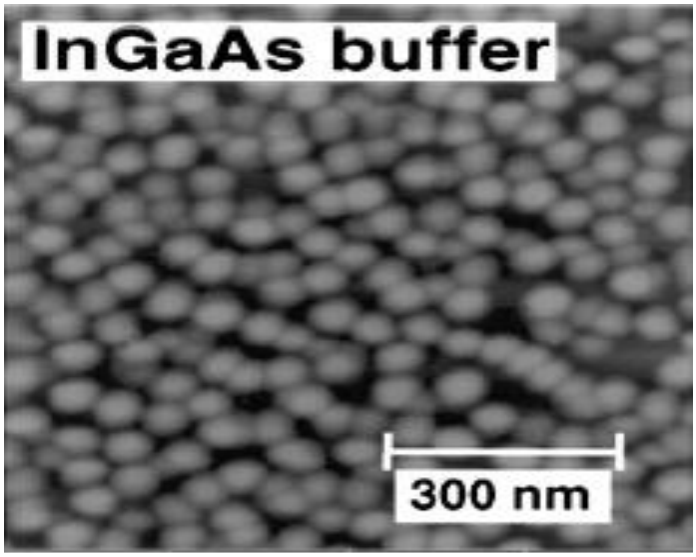

Fig. 4. InGaAs self-assembled dots on GaAs substrate [31].

2.2 Selective Area Epitaxy

Patterning of QDs is very important in order to control the size and position of each dot in order to fully utilize their properties. In selective area epitaxy, silicon dioxide or silicon nitride is used to inhibit the growth in the masked region. Typically a layer of silicon dioxide is grown and the dots are transferred to the oxide by electron beam lithography. Since the selective area epitaxy process involves e-beam lithography, it is expensive while writing dots on a large sample for making lasers. Another major issue is growth enhancement in the unmasked region near the edges due to lateral diffusion of the precursors. In case of the InGaAs quantum dots, indium

segregation will occur, which will lead to an increase in the indium content in the unmasked regions. Since the emission wavelength for a laser is highly dependent on the indium content and size of the dot, any change in the indium content or the size of the dot can affect the emission wavelength. Another problem is the uncertain dot size because of beam spreading and scattering from the poly methyl methacrylate (PMMA) substrate. A 5 nm square will round approximately to 45 nm diameter circles after the development of PMMA. The minimum center-to-center spacing successfully achieved is 70 nm. Pitches below 70 nm cannot be achieved because of the limitation of e-beam lithography. It is very difficult to find the correct dose even for 70 nm spacing. Although the positioning of dots can be controlled well enough, there are some problems with the growth enhancement that change the emission wavelength. Figure 5 shows an overview of selective area epitaxy and growth enhancement.

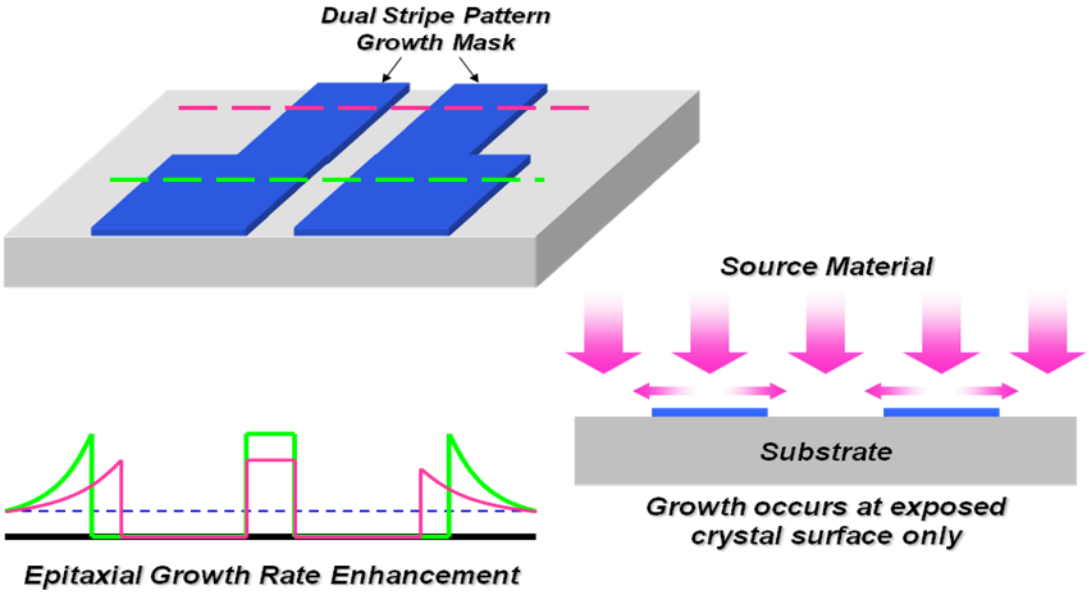

Fig. 5. Overview of selective area epitaxy.

Room temperature operation of quantum dot lasers fabricated by selective area epitaxy has been demonstrated [32]. Figure 6 shows the atomic force microscopic (AFM) image of dots

with 75 nm pitch fabricated by selective area epitaxy. From the figure we can see the high uniformity in dot size and position.

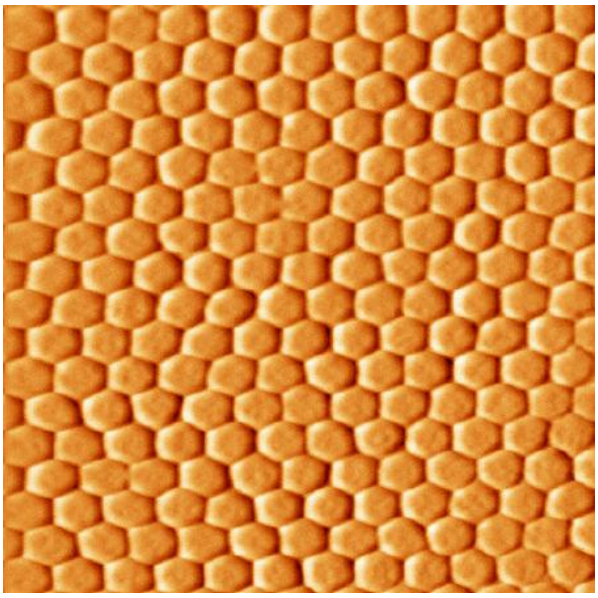

Fig. 6. AFM image of 75 nm pitch dots.

To overcome the problems of growth and composition enhancement, a new wet etch technique has been developed. Since the wet etch technique is a top-down approach which requires no regrowth step, the problem of composition and growth enhancement is eliminated.

2.3 Wet Etch Technique Using Titanium Mask

The growth was carried out in a Thomas Swan, vertical chamber, atmospheric pressure MOCVD reactor. The structure was grown on an n+ (100) GaAs substrate and consists of a 100 nm Si doped n+ GaAs buffer layer, 1 µm Si-doped n-type $Al_{0.75}Ga0._{25}As$ carrier confinement layer, and 100 nm intrinsic GaAs barrier layer. All the layers up to lower barrier were grown at a temperature of 800 °C, which has been established for optimum growth of n-type AlGaAs to reduce incorporation of carbon that can compensate for Si doping. The sample was then transferred to a plasma enhanced chemical vapor deposition (PECVD) system and 50 nm of SiO_2

was deposited. The sample was then spin-coated with AZ-5214 photoresist and alignment targets were defined using negative lithography. The sample was then developed in AZ-327 tetraethyl-ammonium-hydroxide solution and transferred to an evaporation chamber. To aid adhesion, 10 nm of titanium and 150 nm of gold were deposited for alignment targets. The sample was then rinsed in acetone to promote lift-off of the metals. These alignment targets were used during e-beam lithography and subsequent laser processing. The sample was returned to the PECVD system and an additional 50 nm of SiO_2 was deposited to encapsulate the alignment targets. This oxide is deposited to prevent the disintegration of gold and help prevent its contamination during further processing. The sample was then spin-coated with AZ-5214 photoresist, and lithography was done to etch the oxide from the regions except the alignment targets. Figure 7 shows the layout of alignment targets.

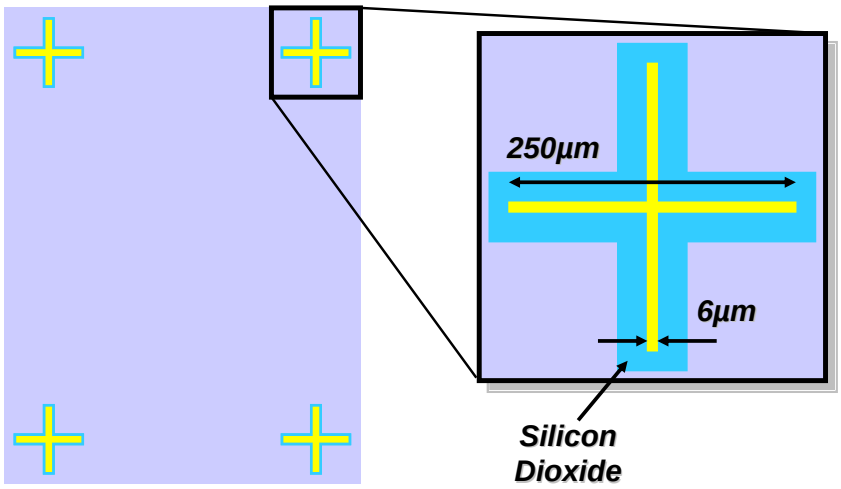

Fig. 7. Layout of alignment targets for e-beam lithography and further processing.

The underlying oxide was etched with a buffered hydrofluoric acid solution for 30 s. For e-beam preparation the sample was hard-baked at 200 °C for 2 minutes. The sample was then spin-coated with 2% PMMA diluted with anisole at 4000 RPM. The sample was soft-baked at 200 °C for 2 minutes and loaded in JEOL JBX-6000 series electron beam lithography tool to define the

dot pattern. After exposure the sample was developed in 1:2 MIBK: IPA at a temperature of 10 °C. The sample was then rinsed in IPA and blown dry with N_2. The sample was transferred to an evaporation tool and 10 nm of Ti was evaporated. The sample was then soaked in 1:1 solution of DCM:CH_3OH for three hours to perform metal lift-off. The resulting Ti dot pattern was used as a mask to wet etch into the underlying quantum well.

Dry etching is known to induce damage to the quantum well. Therefore, to minimize the damage, wet etching was used. The etch begins by removal of any native oxide. The native oxide was etched in 1:1 solution of HCl:H_2O for 15 s. Immediately after, the sample was etched in 50:1 solution of $C_6H_8O_7$:H_2O_2 for 30 s to achieve the required etch depth. The sample was slightly over etched to ensure full transfer of pattern on the quantum well. After etching, spots of the order of a few nm were seen on the surface. To remove the spots the sample was rinsed in H_2O_2 for 15 s and then etched in 1:1 HCl:H_2O for 15 s. The sample was found to be clean after the second etching. A Ti mask was then etched in buffered HF for 1 min. The dots were then inspected under SEM. Figure 8 shows the dot pattern obtained by using a wet etch Ti mask.

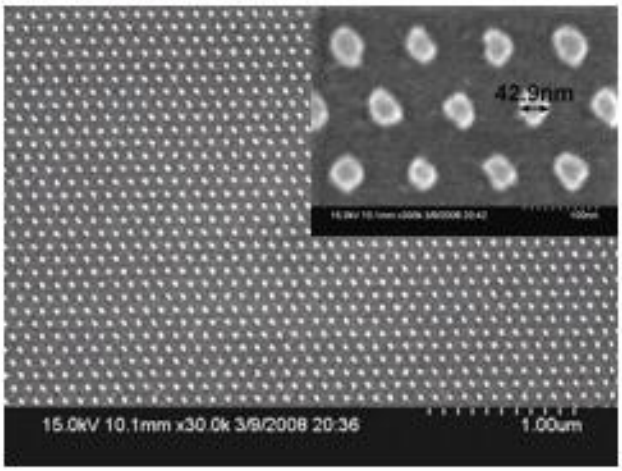

Fig. 8. Wet etch dots fabricated using Ti mask.

2.4 Motivation for New Wet Etch Technique

From Figure 8 we can see that the dots have rough edges due to the metal lift-off involved. In order to have better uniformity, a different approach was used to pattern dots. Alignment targets were defined on the sample as discussed in the previous section. The sample was then transferred to PECVD and 10 nm of SiO_2 was deposited. PMMA was then spun and the sample was loaded in the JEOL JBX-6000 e-beam tool. E-beam files were modified in order to define a mesh pattern instead of a dot pattern. The sample was then developed in 1:2 MIBK:IPA. PMMA was used as an etch mask to transfer the pattern to the oxide. Figure 9(a) shows the dot pattern in the oxide. The sample was then rinsed in methylene chloride and acetone to strip the PMMA. The underlying oxide was used as a wet etch mask to etch into the quantum well. Figure 9 (b) shows the quantum dot pattern after wet etching into the quantum well. This figure shows the better uniformity of dots compared to the previous wet etched dots.

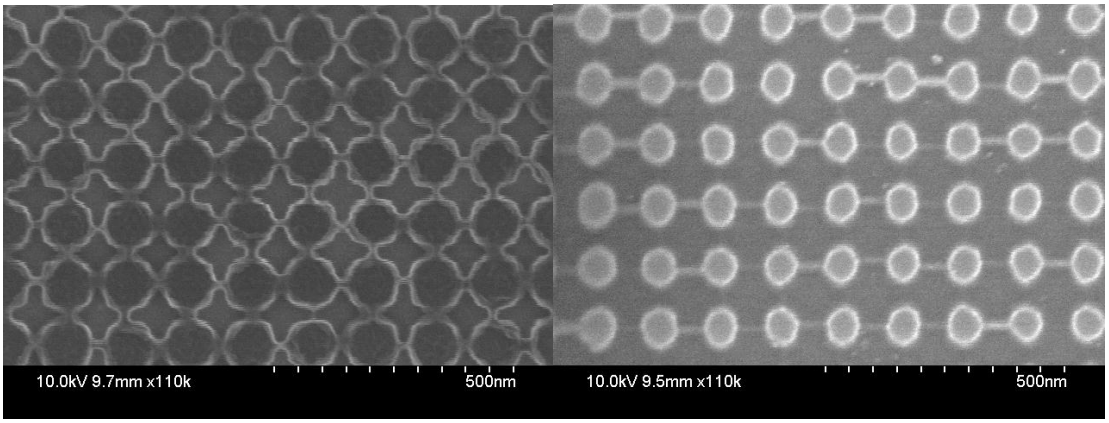

(a) (b)

Fig. 9. (a) Oxide pattern and (b) quantum dot pattern.

2.5 Nanopore Fabrication

In this section, we will discuss the fabrication of a new nanostructure, called a nanopore, which consists of a quantum well which has been periodically perforated and filled with a high bandgap

material. This periodic perturbation can lead to the formation of energy gaps in both conduction and valence bands and has been reported both theoretically and experimentally . The in-plane structure and the three-dimensional structure are illustrated in Figs. 10 and 11 respectively. This unique structure exhibits quantized energy states similar to those of quantum dots but with few fundamental differences. There is a weak in-plane barrier in the nanopore structure, resulting in the formation of energy subbands that correspond to distributed carrier states in contrast to the localized states of a quantum dot. Secondly, the areal fill factor in a nanopore structure is higher than that in quantum dots, leading to a higher effective number of states. This leads to a high achievable gain in the nanopore compared to the quantum dot counterparts.

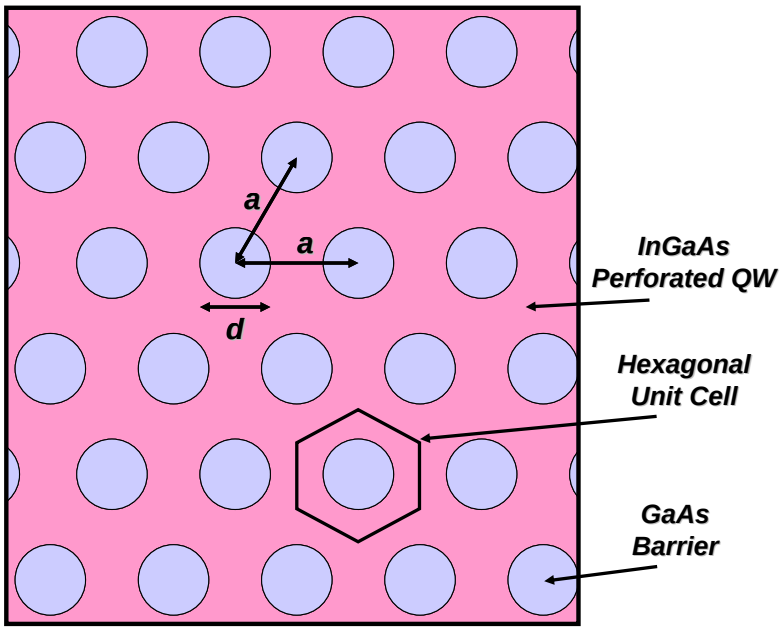

Fig. 10. In-plane geometry of the nanopore structure, where d is the pore diameter and a is the lattice constant .

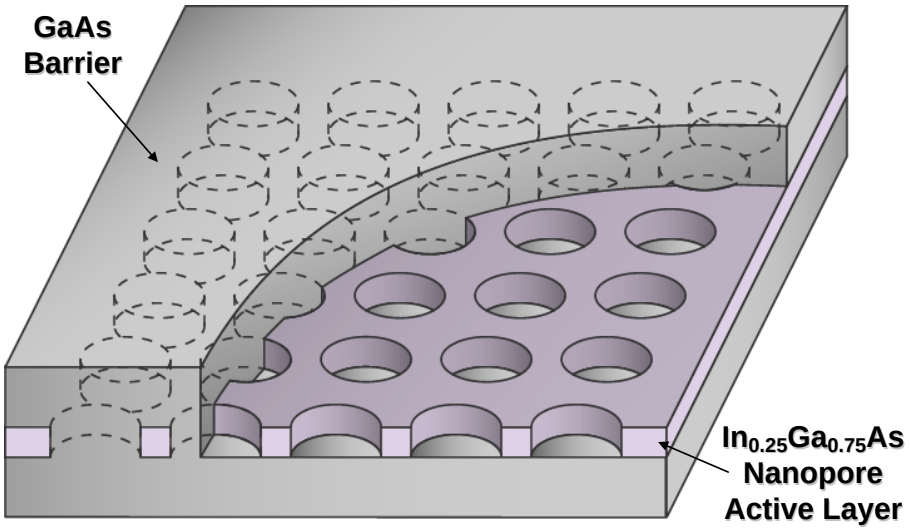

Fig. 11. Three-dimensional illustration of nanopore structure showing the perforation in the quantum well .

The nanopore spectrum is a function of the material composition of the quantum well and the barrier layers, the pore diameter, the pitch between pores and the thickness of the quantum well layer. This represents a wide palette of parameters that can be controlled for achieving the desired gain spectrum. Computational models employing a partial function expansion method have been developed for simulating the band structure of the nanopore active layer. The band diagram of the nanopore is a strong function of pore diameter and pitch and can be tailored by controlling these parameters.

The structure was grown on an n+ (100) GaAs substrate and consists of a 100 nm Si doped n+ GaAs buffer layer, 1 µm Si-doped n-type $Al_{0.75}Ga0._{25}As$ carrier confinement layer, and 100 nm intrinsic GaAs barrier layer. The active region was an 8.7 nm $In_{0.31}Ga_{0.69}As$ quantum well. A 4 nm GaAs cap was then grown to protect the quantum well from damage during subsequent processing steps. The base structure up to the confinement layer was grown at a temperature of 800 °C and then the temperature was reduced to 625 °C for the growth of the lower barrier layer and active region. A 30 nm layer of SiO_2 was deposited by PECVD. AZ-

5214E photoresist was then spun on the sample at 3000 rpm for defining the alignment targets using negative photolithography. The sample was then placed in an evaporator, and 10 nm of Ti and 150 nm of Au were deposited. Ti was deposited to promote the adhesion of gold to SiO_2. The sample was then placed in acetone to promote the lift-off of metals. After lift-off, another 20 nm of SiO_2 was deposited to encapsulate the alignment targets. The silicon dioxide on top helps prevent disintegration of the targets during the e-beam and hence prevents contamination of the sample during subsequent processing steps.

The sample was then baked at 200 °C for 2 min and then spin-coated with 2% PMMA diluted in anisole at 4000 rpm. The sample was then soft-baked at 200 °C for 2 min. The sample was loaded into the e-beam tool to define the desired nanopore pattern on the PMMA. After the e-beam exposure, the sample was developed in 1:2 MIBK:IPA for 3 min at 10 °C to fully transfer the pattern into the PMMA. The sample was then rinsed in IPA for 30 s and blown dry with N_2. The pattern from the PMMA was transferred to oxide by a combination of dry and wet etching. Due to the porosity of the PMMA, it cannot be used as a mask for wet etching. Also, dry etching cannot be used because of the damage induced on the active region, degrading its optical properties. The sample was first dry-etched in a Freon-based reactive ion system for 0.8 min. The etch depth was calibrated to be 30 nm. The sample was then rinsed in methylene chloride for 5 min at 70 °C to strip the PMMA. After stripping the PMMA the sample was rinsed in acetone, menthanol and IPA for 5, 2 and 2 min, respectively, to remove any residue on the sample. The sample was then wet-etched in buffered HF (50:1 NH_4F:HF) to fully transfer the pattern into the oxide. Figure 12(a) shows the nanopore pattern in an oxide template. After defining the oxide pattern, the same wet etching technique as mentioned in the previous section was used to transfer the pattern to the active region. The sample was slightly over-etched to ensure full transfer of the

pattern. The oxide pattern was then etched in BHF and blown dry with N_2. Figure 12(b) shows the nanopore pattern.

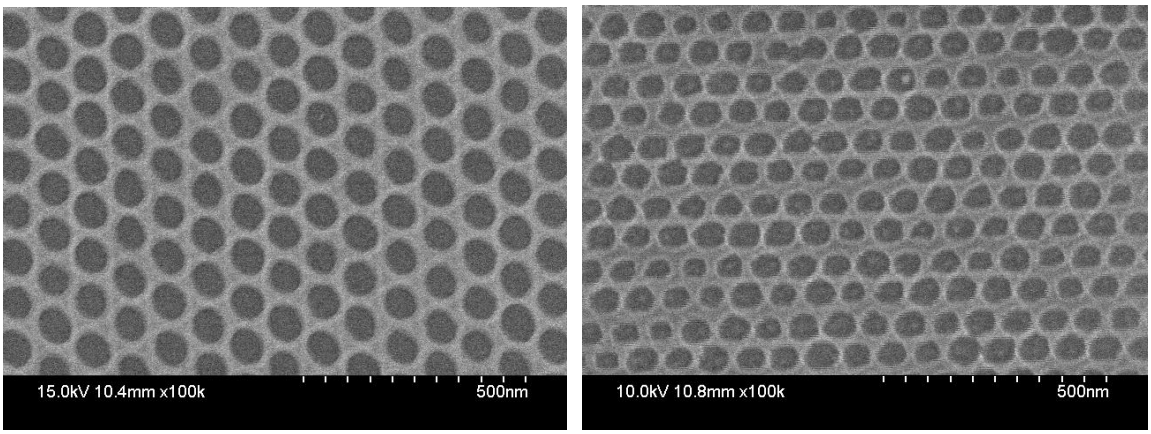

(a) (b)

Fig. 12. (a) Oxide pattern and (b) nanopore pattern.

2.6 Sample Preparation for Photoluminescence

The optical properties of the quantum dot and nanopore nanostructures were studied by photoluminescence measurements. After transferring the nanostructure pattern into the quantum well, regrowth was done to cap the entire structure. The sample was rinsed in 1:1 HCl:H_2O for 15 s to remove the native oxide and then loaded into the reactor. The entire regrowth was performed at 600 °C in order to prevent the disintegration of the dots. The regrowth step consists of growth of a 50 nm GaAs cap, 20 nm $Al_{0.75}Ga_{0.25}As$ barrier and a final 5 nm GaAs cap. The GaAs acts as a barrier for the quantum well and most of the pump intensity is absorbed in the upper and lower GaAs barrier. Carriers are generated in the GaAs barriers which then fall into the lower potential quantum well. The $Al_{0.75}Ga_{0.25}As$ barrier helps improve the confinement of the carriers to the quantum well. The final GaAs cap is to prevent the oxidation of $Al_{0.75}Ga_{0.25}As$.

Figure 13 shows the epitaxial structure of the sample used for photoluminescence measurements.

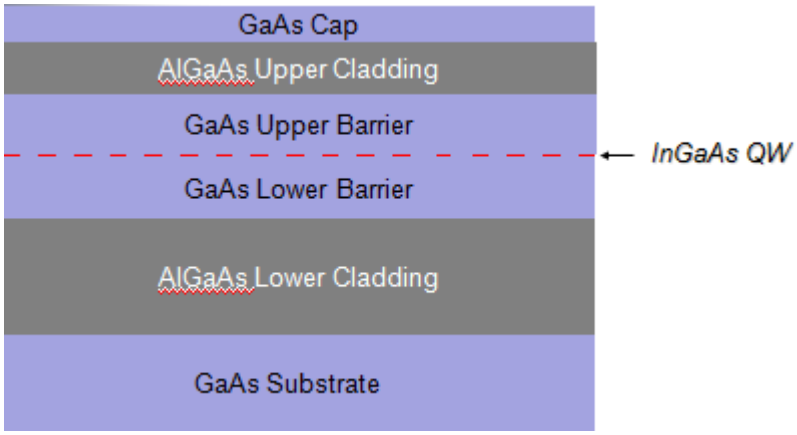

Fig. 13. Epitaxial structure for nanopore and quantum dots.

The sample was spin-coated with AZ-5214 resist and lithography was done to open up 40 × 40 µm apertures on top of the regions consisting of active nanopore or quantum dot layers. The sample was then transferred to an evaporator, and 10 nm of Ti and 150 nm of Au were deposited. The samples were then soaked in acetone to promote lift-off of metals from the aperture regions. The end sample contains a 40 × 40 µm aperture opened up in gold, consisting of nanopore or quantum dot structures.

CHAPTER 3: RESULTS AND DISCUSSION

After quantum dots and nanopores are fabricated, their optical properties are characterized by photoluminescence. In this chapter we will discuss the experimental setup for photoluminescence and some of the results obtained from this setup.

3.1 Photoluminescence

Photoluminescence is a process in which a photon absorbed by the semiconductor material is reradiated. It is a non-destructive way of probing the optical properties of a material. The device under test is excited with the photons having energy greater than the bandgap of the material. The sample then reradiates the photons close to the bandgap or quantum states. The intensity and the spectrum obtained from photoluminescence can reflect various material properties. Some of the uses of photoluminescence include the determination of bandgap, impurity level and defect detection, recombination mechanisms and material quality. Whenever the material under test is excited, photons cause the electrons to move to excited states. The energy of the emitted photon can be related to the difference between two states, i.e., between the conduction band state and the valence or quantum state. This can give sufficient information about the bandgap of the new materials. During the photoexcitation, carriers are injected not only into the excited states but also into defect states if any are present in the material. The sub- bandgap emissions can then be used to determine the position of the defect states, and the intensity of the photoemission determines the density of defect states. Photoluminescence can also be used to determine the type of the recombination in the semiconductor material. The recombination can either be radiative or non-radiative. The intensity of the photoemission and its dependence on temperature can be directly related to the type of recombination mechanism in the semiconductor material. Also, the intensity of the photoemission determines whether the material is of optical quality.

3.2 Experimental Setup

Quantum dot and nanopore samples were pumped with the 488 nm line of an Ar-ion laser. The beam spot was focused to a size of approximately 100 μm. The luminescence from the sample was collected with a 0.5 numerical aperture objective lens and was directed to a 1 m long monochromator having a spectral resolution of 2 nm. The signal was then measured using a liquid nitrogen cooled Ge detector and a lock-in amplifier. Figure 14 shows the schematic of the setup initially used to measure the photoluminescence. The initial setup used to measure the photoluminescence had different lenses for sample illumination and luminescence collection.

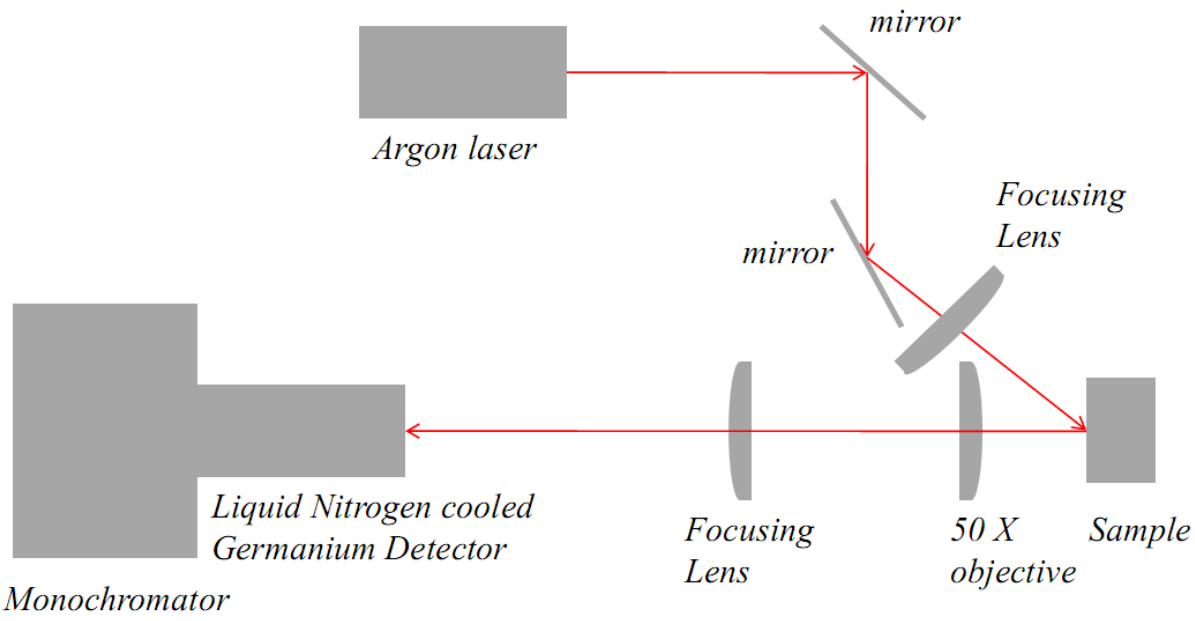

Fig. 14. Schematic layout of the initial setup used for measuring the photoluminescence.

One of the major limitations of this setup is that since the input beam and collection optics do not share the same optical path, alignment becomes quite complicated. Also, the spot size is approximately 100 μm, so measurement of samples with small apertures is difficult. Recall that the quantum dot and nanopore samples were patterned in 40 μm × 40 μm squares. Therefore,

measurement of these samples became very difficult with the current setup. Confocal microscopy was used to resolve smaller samples. In the new setup the excitation and collection of the luminescent light were done through a single microscope objective instead of two lenses as used in the previous setup. Figure 15 shows the layout of the new setup.

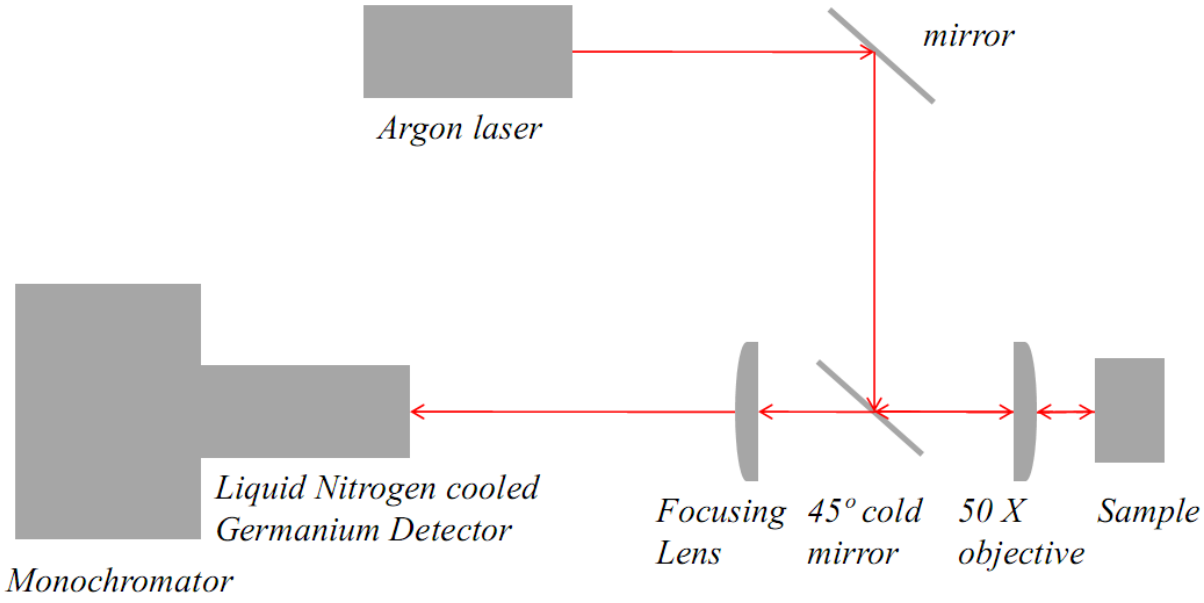

Fig. 15. Confocal microscopy setup.

The light from the Ar-ion laser is directed towards a 45º cold mirror. The cold mirror has a reflectivity in the range of 400-700 nm and has 85% transmission from 780-2500 nm. The visible laser light reflected from the cold mirror is then focused by a 50× objective lens onto the sample. The spot size of the beam is approximately 20 µm. Since the excitation and collection of the luminescent light is done through the same objective lens, alignment is not a problem. The luminescent light from the sample is focused towards a 1 m long monochromator. Figure 16 shows the schematic layout monochromator. The f-number of the focusing lens is matched to the f-number of the parabolic mirror inside the monochromator so that a focused beam reaches the parabolic mirror. A dispersive grating controlled by a stepper motor is used to direct the light

towards the second parabolic mirror. The second parabolic mirror focuses the light on the exit slit, which has a liquid nitrogen cooled germanium detector attached at the output. The spectral resolution of the monochromator is adjusted by controlling the entrance and exit slit separation. The spectrum can be resolved to within 1 Å.

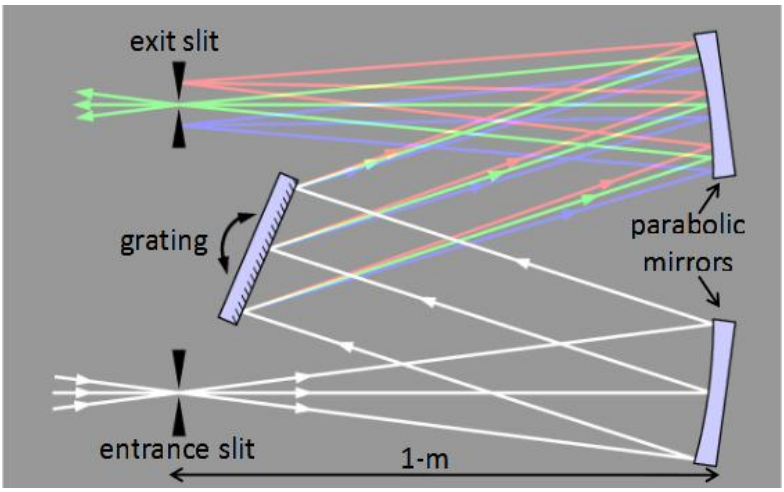

Fig. 16. Layout of the parabolic mirrors and grating inside the monochromator.

3.3 Results and Discussion

Photoluminescence measurements were done at 77 K using an argon-ion pump laser operating at 488 nm and a nitrogen cooled Ge-detector. Figure 17 shows a comparison between a reference quantum well (QW) and a nanopore lattice with an 80 nm pitch and 60 nm pore diameter.

Peak emission from the QW shows the ground and first excited states at 1008 nm and 928 nm. The nanopore emission is blue-shifted relative to the quantum well with peaks at 1004 nm and 924 nm. Finite-element simulations were performed to calculate the emission spectra of the nanopore lattice and good agreement is observed between the theoretical calculations and experimental results. The increased emission from the excited state is direct evidence of the retarded carrier cooling process in the nanopore.

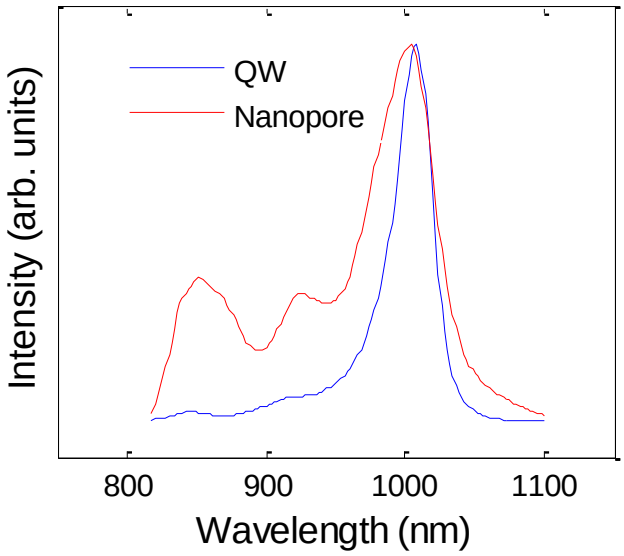

Fig.17. PL spectra for quantum well and 80 nm nanopore lattice with 60 nm pore diameter.

Figure 18 shows the PL spectra for five nanopore lattices with pitch of 80 nm and pore diameters of 50, 55, 60, 65 and 70 nm respectively. As the pore diameter is increased, the peak wavelength undergoes a blue-shift as shown in Figure 19. This can be attributed to the increasing wavefunction overlap with the barrier material as the pore diameter is increased. The in-plane periodic potential leads to the formation of mini-subbands, as predicted earlier, leading to the widening in the emission peak centered at 1004 nm. Further broadening of the lineshape can also be attributed to non-uniformity of nanopore geometry due to processing variations. Theoretical calculations predict the subband separation to be of the order of a few meV, making it difficult to clearly delineate the in-plane subbands in the PL measurements at 77 K.

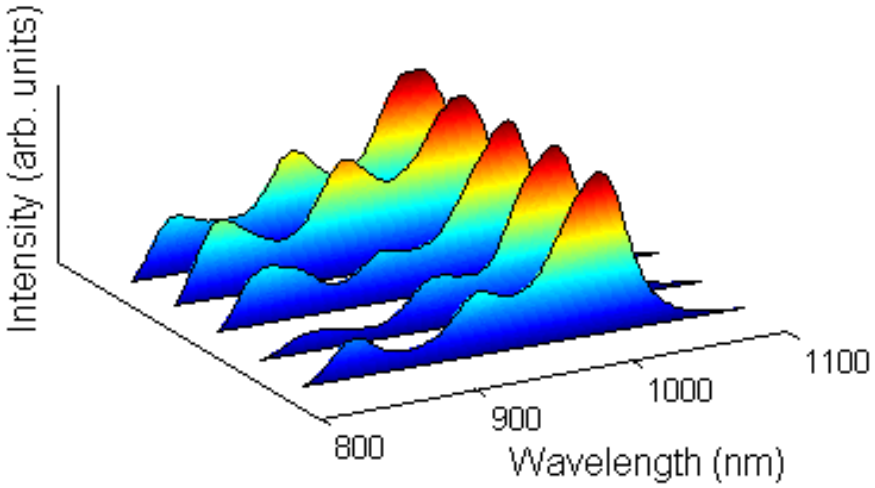

Fig. 18. PL spectra of nanopore lattices with pore diameters of 50, 55, 60, 65 and 70 nm on 80 nm pitch.

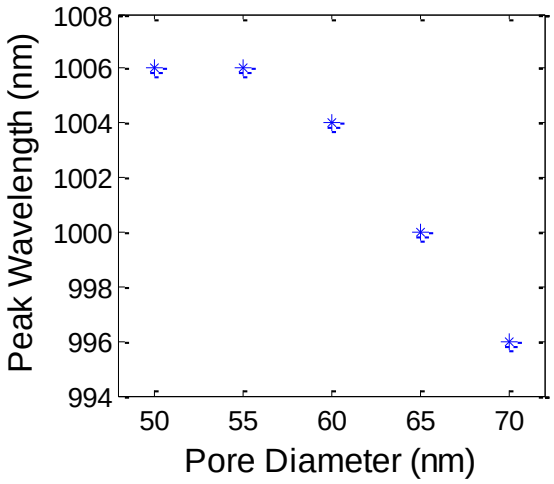

Fig. 19. Peak emission wavelength vs. pore diameter for 80 nm pitch pattern.

The ratio of the emission from the excited state to the ground state increases with pore diameter. Depopulation of electrons injected into the higher subbands proceeds by either spontaneous recombination or relaxation into lower subbands. From symmetry considerations, the effects of the nanopore periodicity on the valence and conduction band wavefunctions are identical, leading to almost no change in the spontaneous emission probability. This implies that

the intersubband scattering rate decreases significantly in the nanopore with increasing pore diameter.

REFERENCES

[1] D. L. Huffaker, G. Park, Z. Zou, O. B. Shchekin, and D. G. Deppe, "Continuous-wave low-threshold performance of 1.3- μm InGaAs-GaAs quantum-dot lasers," *IEEE Journal of Selected Topics in Quantum Electronics*, vol. 6, pp. 452-461, 2000.

[2] F. Heinrichsdorff, M.-H. Mao, N. Kirstaedter, A. Krost, D. Bimberg, A. O. Kosogov, and P. Werner, "Room-temperature continuous-wave lasing from stacked InAs/GaAs quantum dots grown by metalorganic chemical vapor deposition," *Applied Physics Letters*, vol. 71, pp. 22-24, 1997.

[3] R. L. Sellin, C. Ribbat, M. Grundmann, N. N. Ledentsov, and D. Bimberg, "Close-to-ideal device characteristics of high-power InGaAs/GaAs quantum dot lasers," *Applied Physics Letters*, vol. 78, pp. 1207-1209, 2001.

[4] D. A. Livshits, A. R. Kovsh, N. A. Maleev, A. E. Zhukov, V. M. Ustinov, N. N. Ledentsov, Z. I. Alferov, D. Bimberg, G. Lin, and J. Chi, "High-performance of single mode InAs/InGaAs/GaAs quantum dot lasers of 1.3-micron range," in *Quantum Sensing: Evolution and Revolution from Past to Future*, 2003, pp. 524-530.

[5] N. A. Maleev, A. R. Kovsh, A. E. Zhukov, S. S. Mikhrin, A. V. Vasil'ev, E. S. Semenova, Y. M. Shernyakov, E. V. Nikitina, N. V. Kryjanovskaya, D. S. Sizov, I. P. Soshnikov, M. V. Maximov, N. N. Ledentsov, V. M. Ustinov, D. Bimberg, and Z. I. Alferov, "MBE growth of low-threshold long-wavelength QD lasers on GaAs substrates," in *The 10th International Symposium on Nanostructures: Physics and Technology*, 2002, pp. 357-360.

[6] D. L. Huffaker, G. Park, Z. Zhou, O. B. Shchekin, and D. G. Deppe, "1.3 μm room-temperature GaAs-based quantum-dot laser," *Applied Physics Letters*, vol. 73, pp. 2564-2566, 1998.

[7] A. R. Kovsh, N. A. Maleev, A. E. Zhukov, S. S. Mikhrin, A. R. Vasil'ev, Y. M. Shemyakov, M. V. Maximov, D. A. Livshits, V. Ustinov, Z. I. Alferov, N. N. Ledentsov, and D. Bimberg, "InAs/InGaAs/GaAs quantum dot lasers of 1.3 μm range with high (88%) differential efficiency," *Electronics Letters*, vol. 38, pp. 1104-1106, 2002.

[8] C. Ribbat, R. L. Sellin, I. Kaiander, F. Hopfer, N. N. Ledentsov, D. Bimberg, A. R. Kovsh, V. M. Ustinov, A. E. Zhukov, and M. V. Maximov, "Complete suppression of filamentation and superior beam quality in quantum-dot lasers," *Applied Physics Letters*, vol. 82, pp. 952-954, 2003.

[9] M. Kamp, M. Schmitt, J. Hofmann, F. Schafer, J. P. Reithmaier, and A. Forchel, "InGaAs/AlGaAs quantum dot DFB lasers operating up to 213 °C," *Electronics Letters*, vol. 35, pp. 2036-2037, 1999.

[10] D. Loss and D. P. DiVincezo, "Quantum computing with quantum dots," *Physical Review A*, vol. 57, pp. 120-126, 1998.

[11] R. J. Ellingson, M. C. Beard, J. C. Johnson, P. Yu, O. I. Micic, A. J. Nozik, A. Shabaev, and A. L. Efros, "Highly efficient multiple exciton generation in colloidal PbSe and PbS quantum dots," *Nano Letters*, vol. 5, pp. 865-871, 2005.

[12] D. S. Boudreaux, F. Williams, and A. J. Nozik, "Hot carrier injection at semiconductor electrolyte junctions," *Journal of Applied Physics*, vol. 51, p. 2158, 1980.

[13] J. Nelson, *The Physics of Solar Cells*. London, UK: Imperial College Press, 2003.

[14] H. J. Queisser, "Detailed balance limit for solar cell efficiency," *Materials Science and Engineering: B*, vol. 159-160, pp. 322-328, 2009.

[15] J. Zhao, A. Wang, M. A. Green, and F. N. Ferrazza, "19.8% efficient honeycomb textured multicrystalline and 24.4% monocrystalline silicon solar cells," *Applied Physics Letters*, vol. 73, pp.1991-1993, 1998.

[16] T. Takamoto, T. Agui, K. Kamimura, and M. Kaneiwa, "Multijunction solar cell technologies- High efficiency, radiation resistance, and concentrator applications," in *Proceedings of the 3rd World Conference on Energy Conversion*, Osaka, Japan, 2003, vol. 1, pp. 581-586.

[17] P. Wurfel, "Thermodynamic limitations to solar energy converstion," *Physica E: Low-Dimensional Systems and Nanostructures*, vol. 14, pp. 18-26, 2002.

[18] G. F. Brown and J. Wu, "Third generation photovoltaics," *Laser & Photonics Revision* 3, vol. 4, pp. 394-405, 2009.

[19] R. R. King, D. C. Law, K. M. Edmondson, C. Fetzer, G. S. Kinsey, H. Yoon, R. A. Sherif, and N. H. Karam, "40% efficient metamorphic GaInP/GaInAs/Ge multijunction solar cells," *Applied Physics Letters*, vol. 90, p. 183516, 2007.

[20] A. Luque, A. Marti, and L. Cuadra, "Thermodynamic consistency of sub-bandgap absorbing solar cell proposals," *IEEE Transactions on Electron Devices*, vol. 48, pp. 2118-2124, 2001.

[21] G. Conibeer, M. Green, R. Corkish, Y. Cho, E. Cho, C. Jiang, T. Fangsuwannarak, E. Pink,Y. Huang, T. Puzzer, T. Trupke, B. Richards, A. Shalav, and K. Lin, "Silicon nanostructures for third generation photovoltaic applications," *Thin Solid Films*, vol. 511, pp. 654-662, 2006.

[22] C. V. Shank, R. L. Fork, R. F. Leheny, and J. Shah, "Dynamics of photoexcited GaAs band-edge absorption with subpicosecond resolution," *Physical Review Letters*, vol. 42, pp. 112-115, 1979.

[23] V. B. Campos, S. Das Sarma, and M. A. Stroscio, "Phonon-confinement effect on electron energy loss in one dimensional quantum wires," *Physical Review B*, vol. 46, pp. 3849-3853, 1992.

[24] R. J. Ellingson, M. C. Beard, J. C. Johnson, P. Yu, O. I. Micic, A. J. Nozik, A. Shabaev, and A. L. Efros, "Highly efficient multiple exciton generation in colloidal PbSe and PbS quantum dots," *Nano Letters*, vol. 5, pp. 865-871, 2005.

[25] R. Schaller, M. Sykora, J. Pietryga, and V. Klimov, "Seven excitons at a cost of one: Redefining the limits for conversion efficiency of photons into charge carriers," *Nano Letters*, vol. 6, pp. 424-429, 2006.

[26] V. C. Elarde, R. B. Swint, T. S. Yeoh, and J. J. Coleman, "Fabrication of InGaAs quantum dots by metal organic chemical vapor deposition and selective area epitaxy," in *Conference on Lasers and Electro-Optics*, 2004.

[27] D. A. Livshits, A. R. Kovsh, N. A. Maleev, A. E. Zhukov, V. M. Ustinov, N. N. Ledentsov, Z. I. Alferov, D. Bimberg, G. Lin, and J. Chi, "High-performance of single mode InAs/InGaAs/GaAs quantum dot lasers of 1.3-micron range," in *Quantum Sensing: Evolution and Revolution from Past to Future*, 2003, pp. 524-530

[28] R. L. Sellin, I. Kaiander, D. Ouyang, T. Kettler, U. W. Pohl, D. Bimberg, N. D. Zakharov, and P. Werner, "Alternative-precursor metalorganic chemical vapor deposition of self-organized InGaAs/GaAs quantum dots and quantum-dot lasers," *Applied Physics Letters*, vol. 82, pp. 841-843, 2003.

[29] M. J. da Silva, A. A. Quivy, S. Martini, T. E. Lamas, E. C. F. da Silva, and J. R. Leite, "InAs/GaAs quantum dots optically active at 1.5μm," *Applied Physics Letters*, vol. 82, p. 2646, 2003.

[30] Y. Q. Wei, S. M. Wang, F. Ferdos, J. Vukusic, Q. X. Zhao, M. Sadeghi, and A. Larsson, "Aluminum incorporation for growth optimization of 1.3μm emission InAs/GaAs quantum dots by molecular beam epitaxy," *Journal of Crystal Growth*, vol. 251, p. 172, 2003.

[31] D. L. Huffaker, G. Park, Z. Zou, O. B. Shchekin, and D. G. Deppe, "Continuous-wave low-threshold performance of 1.3- μm InGaAs-GaAs quantum-dot lasers," *IEEE Journal of Selected Topics in Quantum Electronics*, vol. 6, pp. 452-461, 2000.

[32] V. C. Elarde, R. Rangarajan, J. J. Borchardt, and J. J. Coleman, "Room temperature operation of patterned quantum-dot laser fabricated by electron beam lithography and selective area metal-organic chemical vapor deposition," *Photonics Technology Letters*, vol. 17, pp. 935-937, 2005.